Key Points:
- First results of FUV stellar occultations taken with the IUVS instrument onboard MAVEN
- Temperature profiles reveals that the lower thermosphere is significantly cooler than predicted
- Detection of CO_2 and O_2 number densities

Probing the Martian atmosphere with MAVEN/IUVS stellar occultations

H. Gröller[1], R. V. Yelle[1], T. T. Koskinen[1], F. Montmessin[2], G. Lacombe[2], N. M. Schneider[3], J. Deighan[3], A. I. F. Stewart[3], S. K. Jain[3], M. S. Chaffin[3], M. M. J. Crismani[3], A. Stiepen[3], F. Lefèvre[2], W. E. McClintock[3], J. T. Clarke[4], G. M. Holsclaw[3], P. R. Mahaffy[5], S. W. Bougher[6], and B. M. Jakosky[3]

[1]Lunar and Planetary Laboratory, University of Arizona, Tucson, Arizona, USA, [2]LATMOS, Université Versailles Saint-Quentin/CNRS, Guyancourt, France, [3]Laboratory for Atmospheric and Space Physics, University of Colorado Boulder, Boulder, Colorado, USA, [4]Center for Space Physics, Boston University, Boston, Massachusetts, USA, [5]Goddard Space Flight Center, Greenbelt, Maryland, USA, [6]Department of Atmospheric, Oceanic, and Space Sciences, University of Michigan, Ann Arbor, Michigan, USA

Abstract The first campaign of stellar occultations with the Imaging Ultraviolet Spectrograph (IUVS) instrument on board of Mars Atmosphere and Volatile EvolutioN (MAVEN) mission was executed between 24 and 26 March 2015. From this campaign 13 occultations are used to retrieve CO_2 and O_2 number densities in the altitude range between 100 and 150 km. Observations probe primarily the low-latitude regions on the nightside of the planet, just past the dawn and dusk terminator. Calculation of temperature from the CO_2 density profiles reveals that the lower thermosphere is significantly cooler than predicted by the models in the Mars Climate Database. A systematically cold layer with temperatures of 105–120 K is seen in the occultations at a pressure level around 7×10^{-6} Pa.

1. Introduction

Spacecraft observations of UV stellar occultations have proved to be a powerful technique for the study of upper atmospheric structure and composition. Stellar occultation observations by the Spectroscopy for Investigation of Characteristics of the Atmosphere of Mars (SPICAM) spectrograph on Mars Express (MEX) have been used to map the distribution of CO_2, O_3, aerosols, and temperature [*Montmessin et al.*, 2006b, 2006a; *Lebonnois et al.*, 2006; *Forget et al.*, 2009; *McDunn et al.*, 2010; *Montmessin*, 2013] in the Martian upper atmosphere providing important constraints on the circulation and physical processes controlling atmospheric structure. More recently, *Sandel et al.* [2015] identified the signature of O_2 in the SPICAM occultation measurement and inferred O_2 mole fractions from 1×10^{-3} to 5×10^{-3} in the 90–120 km altitude range. One of the principal results of these investigations is that the upper atmosphere of Mars is highly variable, requiring dense sampling in important geophysical variables (latitude, longitude, local time, solar activity, L_S, etc.) to be adequately understood.

The Imaging Ultraviolet Spectrograph (IUVS) on Mars Atmosphere and Volatile EvolutioN (MAVEN) mission is designed to observe stellar occultations in both the FUV and MUV channels. The FUV measurements are sensitive to CO_2, O_2, and potentially clouds and aerosols, while the MUV are sensitive to CO_2, O_3, and clouds and aerosols. The first occultation campaign was carried out on 24–26 March 2015. We report here results from the FUV measurements. The stellar occultations are an important component of the overall MAVEN science goals because they are one of the two techniques (the other being limb profiles of UV emissions) that connect the upper atmosphere (around 110–200 km), probed by the in situ measurements on MAVEN, with the middle atmosphere (around 45–110 km). The IUVS FUV occultations probe altitudes of ~100–150 km corresponding to pressures of 10^{-2} to a few times 10^{-6} Pa. This region is critical to an understanding of the Mars atmosphere because it encompasses the upper mesosphere, the mesopause (~100 km), the homopause (~125 km), and the lower thermosphere. Eventually, if we are able to understand this region, we will have gone a long way toward understanding the processes that control the exospheric temperature. This is critical for atmospheric escape rates, the ultimate goal of the MAVEN investigation. A complete overview of the MAVEN mission can be found in *Jakosky et al.* [2015].

2. IUVS Stellar Occultations

The FUV channel of the IUVS covers the 110 to 190 nm spectral range with an intrinsic spectral resolution of 0.6 nm [*McClintock et al.*, 2014]; however, to reduce the data volume, four spectral pixels are binned to produce an effective sampling of 0.33 nm. Spatial imaging is not necessary for occultations, but 20 spatial lines are returned with each line corresponding to 6 spatial pixels in order to characterize instrument performance and background levels. The stellar signal is strongly concentrated in the central line with the other lines providing a measurement of background signal levels due to stray light and emissions from Mars. The signal is recorded with a cadence of 2.6 s consisting of 2 s of integration time and 0.6 s of overhead (detector readout, etc.). This sampling rate corresponds to an altitude resolution between 1.5 and 4.5 km, depending on the geometry of the particular occultation.

The transmission of the atmosphere is calculated by dividing the spectra observed along lines of sight that penetrate the atmosphere by spectra recorded outside the atmosphere. Absorption signatures are present in the IUVS/FUV occultations up to altitudes of ~160 km; therefore, we use the regions higher than 180 km to define an average unattenuated spectrum. Often, in the analysis of spacecraft occultations, it is necessary to shift the unattenuated spectrum before division to account for spectral shifts associated with changes in spacecraft inertial point during the occultation. The spectral shifts are best determined from the data itself, through the time dependence of wavelength shifts of features in the stellar spectrum. The MAVEN occultations are quite stable, and only in rare cases do we see any evidence for a spectral shift between the reference spectrum and attenuated spectra; thus, this correction is unnecessary for most of the data shown here.

The occultations are observed through the large "keyhole" at the end of the IUVS slit, which has an angular size of 0.69° by 0.90° [*McClintock et al.*, 2014]. Because of the large size of the keyhole it admits significant radiation from the extended emissions from the Mars atmosphere, especially from the bright H Lyman α line at 121.6 nm. This contribution is easily recognized through its extended spatial signature and is subtracted off as background. As the H Lyman α background is also present at lower altitudes and constant with altitude, a mean value over altitudes where all the stellar signal is already absorbed is used for the correction. Background due to stray light and thermal noise on the detector is also subtracted from the data prior to calculation of the transmission, but these corrections are quite small.

The MAVEN stellar occultations are executed in dedicated campaigns that are scheduled to take place every other month. Each campaign lasts for five consecutive orbits, which is equivalent to one planetary rotation and provides complete longitudinal coverage. Different stars (see Table 1 for stars used in the first campaign) are targeted to obtain latitudinal and local time coverage. As they are periods of intense activity, the normal operation of the MAVEN spacecraft is suspended during the execution of these campaigns. In this first campaign a total of 60 occultations during five orbits were attempted by targeting 12 stars during each orbit. Because of an unforeseen timing problem some of the occultations are compromised and only 13 occultations are used here to retrieve CO_2 and O_2 number densities. Only 10 occultations have sufficient altitude sampling to permit calculation of temperature and pressure profiles. Stars, orbit number, and the corresponding geometry of the occultations in the first stellar campaign are listed in Table 1. The data can be found in the Planetary Data System (PDS:http://atmos.nmsu.edu/data_and_services/atmospheres_data/MAVEN/maven_iuvs.html) (PDS) with the filename identifier `v02_r01`. This occultation campaign probes the atmosphere primarily on the nightside of the planet, just past the terminator at equatorial and midlatitude regions. The signal-to-noise ratio (SNR) per spectral bin is ~22 near 130 nm, where the IUVS sensitivity is a maximum and the CO_2 band are detected, decreasing to ~6 near 165 nm where the IUVS sensitivity has fallen to roughly half its peak value.

Our analysis approach builds on previous experience with occultation analysis [*Montmessin et al.*, 2006b; *Koskinen et al.*, 2011; *Capalbo et al.*, 2013; *Sandel et al.*, 2015]. The measured transmission spectra is fitted at each altitude assuming absorption by CO_2 and O_2 and using the Levenberg-Marquardt algorithm to retrieve the best fit column densities. We use CO_2 cross sections in the wavelength range from 106 nm to 192 nm composed from measurements of *Stark et al.* [2007], *Yoshino et al.* [1996], and *Parkinson et al.* [2003]. For O_2 we used again a composed absorption cross section from *Ogawa and Ogawa* [1975], *Lu et al.* [2010], *Yoshino et al.* [2005], and *Minschwaner et al.* [1992]. As no cross sections for the temperature of interest are available, a semilogarithmic extrapolation is used to get absorption cross sections for 130 K. A detailed description of the absorption cross sections and their small sensitivity to the temperature dependency can be found in *Sandel et al.* [2015]. Column density profiles obtained from spectral fits are inverted to get the corresponding local densities by using the Tikhonov regularization method [*Quémerais et al.*, 2006; *Sandel et al.*, 2015]. For the

Table 1. Observation Geometry for Occultations Recorded During the First Stellar Campaign[a]

Star	Orbit (Event #)	Egress/Ingress	UTC Time	Lon [°]	Lat [°]	Ls [°]	SZA [°]	LT [hrs]
λ Sco	00935 (7)	Egress	24 Mar 2015 - 23:43:55.31	−131.71	−38.17	314.07	116.02	21.86
λ Sco	00937 (7)	Egress	25 Mar 2015 - 08:43:40.12	95.91	−36.92	314.28	116.81	21.81
λ Sco	00939 (7)	Egress	25 Mar 2015 - 17:45:16.44	-36.51	−35.28	314.50	117.85	21.76
λ Sco	00941 (7)	Egress	26 Mar 2015 - 02:46:50.76	−168.89	−34.02	314.72	118.63	21.72
λ Sco	00943 (7)	Egress	26 Mar 2015 - 11:48:22.84	58.72	−32.43	314.93	119.59	21.68
α Lyr	00935 (9)	Ingress	25 Mar 2015 - 01:01:56.78	−30.65	8.06	314.10	94.19	5.86
α Lyr	00937 (9)	Ingress	25 Mar 2015 - 10:03:37.09	−163.40	8.45	314.31	95.19	5.80
α Lyr	00939 (9)	Ingress	25 Mar 2015 - 19:05:13.41	63.80	8.88	314.53	96.27	5.73
α Lyr	00941 (9)	Ingress	26 Mar 2015 - 04:06:47.73	−69.07	9.33	314.75	97.41	5.66
α Lyr	00943 (9)	Ingress	26 Mar 2015 - 13:08:19.81	158.12	9.74	314.96	98.47	5.59
β Cep	00935 (10)	Ingress	25 Mar 2015 - 01:38:41.51	−34.60	−17.44	314.11	81.93	6.19
β Cep	00937 (10)	Ingress	25 Mar 2015 - 10:40:22.08	−166.87	−17.45	314.33	82.34	6.16
β Cep	00939 (10)	Ingress	25 Mar 2015 - 19:41:58.40	60.77	−17.46	314.55	82.84	6.13

[a]The given times and geophysical parameters are given for the beginning of the occultations. The used stars are Beta Cephei (β Cep), Lambda Scorpii (λ Sco), and Alpha Lyrae (α Lyr).

vertical inversion, convergence is achieved when the relative difference between the two latest iterations is lower than 10^{-3}. A smoothing coefficient of 0.4 was chosen empirically to balance the smoothing of measurement noise while preserving real atmospheric perturbations.

3. Results

An example of a measured transmission spectra obtained during the occultation of λ Sco on orbit 00943 are shown in Figure 1 (top). The colored lines show the fitted model transmission spectra using CO_2 and O_2 as possible absorbers. Figure 1 (bottom) shows the residuals between models and measurements. With the χ_ν^2 statistics and the F test we are confident that O_2 can be detected. Visual examination of these spectra reveal the presence of an O_2 absorption feature at 120.6 nm as well as the characteristic vibrational structure of the CO_2 bands. The presence of the O_2 feature at 120.6nm confirms the detection of O_2 discussed in *Sandel et al.* [2015] which was based only on the broadband spectral influence seen in the lower resolution SPICAM/MEX spectra.

The CO_2 and the O_2 abundance can be measured for λ Sco, the brightest star in this campaign, but only CO_2 for α Lyr and β Cep. For these fainter stars the H Lyman α airglow transmitted through the keyhole swamps the stellar signal near 120.6 nm and the O_2 absorption feature cannot be measured. The altitude dependent CO_2 and O_2 number density profiles retrieved from the occultations are listed in Table 1 and shown in Figure 2.

Figure 2 also shows densities obtained from the Mars Climate Database (MCD), version 5.2, for the same latitude, longitude, local time, and L_S as for the observations. The MCD is a collection of model predictions using the Laboratoire de Meteorologie Dynamique - General Circulation Model (LMD-GCM) [*González-Galindo et al.*, 2009]. An overview of the Mars Climate Database can be found in *Millour et al.* [2014]. The $F_{10.7}$ solar flux at the time of the first occultation campaign was 138. Because MCD simulations for the current Mars year are not yet available, we compare our results to MCD profiles for the Martian Year (MY) 26 because the average $F_{10.7}$ index for this year (140 – 150) for the L_S = 300 – 330 period is similar to that of the observations. Both observed and model CO_2 densities exhibit significant variability among the different occultations but are roughly consistent within this variability. Our results are also consistent with the Viking measurements [*Nier and McElroy*, 1977] and the recently published O_2 profiles obtained from stellar occultations taken with SPICAM/MEX [*Sandel et al.*, 2015]. Our retrieved O_2 mixing ratios are between 1.5×10^{-3} and 5×10^{-3} which is in agreement with the mixing ratios published recently in *Sandel et al.* [2015] and previous observations by Viking 1 and 2. The O_2 densities inferred from the occultation appear to be systematically lower than predicted by the MCD models, though the difference is smaller than the variability.

The temperature profile for each occultation is calculated by applying the hydrostatic equilibrium constraint to the local CO_2 densities and using the algorithm described in *Snowden et al.* [2013]. Results are shown in Figure 3.
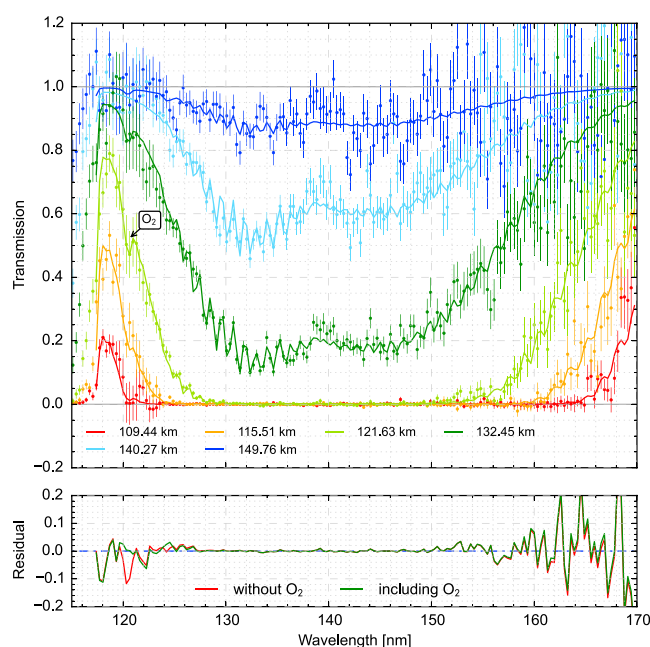
Figure 1. (top) Measured transmission spectra (dots) including their uncertainties (vertical bars) and the model fits (solid lines) for λ Sco orbit number 00943 for several values of the impact point/tangent altitude along the line of sight to the star. The inset indicates the position of the O_2 absorption feature at 120.6 nm. (bottom) The residuals between models and measurements for an altitude of 121.63 km. Including O_2 reduces the residuals where absorption is significant and the F test demonstrate the statistical significance in the residuals.

Calculation of the temperature profile from the density profile also requires specification of an upper boundary condition. We consider several choices. The green curves show calculations based on the assumption that the temperature at the upper boundary is equal to the temperature at the equivalent altitude for models in the MCD corresponding to the latitude, longitude, and local time for the particular occultation. The results are unsatisfactory because, for most profiles, there is a significant difference in slope between the retrieved temperature profile and the MCD profile at the upper boundary leading to large temperature differences at lower
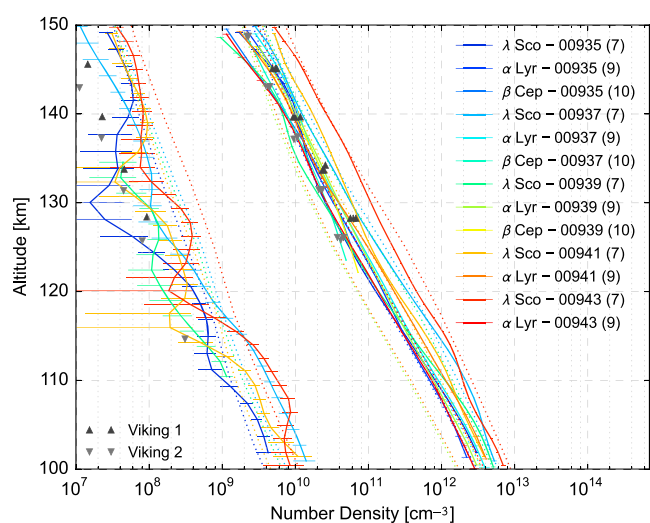

Figure 2. CO_2 and O_2 number densities obtained from IUVS (solid lines) including their uncertainties. For CO_2 some of the formal uncertainties are too small to be seen. In addition, there is a systematic uncertainty of ~10% due to the absorption cross section. Profiles are labeled by the star occulted and MAVEN orbit number the corresponding event number in parentheses. Viking 1 and 2 (gray upright and upside down triangles) measurements taken from *Nier and McElroy* [1977] and modeled profiles from the Mars Climate Database (dotted lines) are also shown. More detail about the Mars Climate Database can be found in *González-Galindo et al.* [2009] and *Millour et al.* [2014].
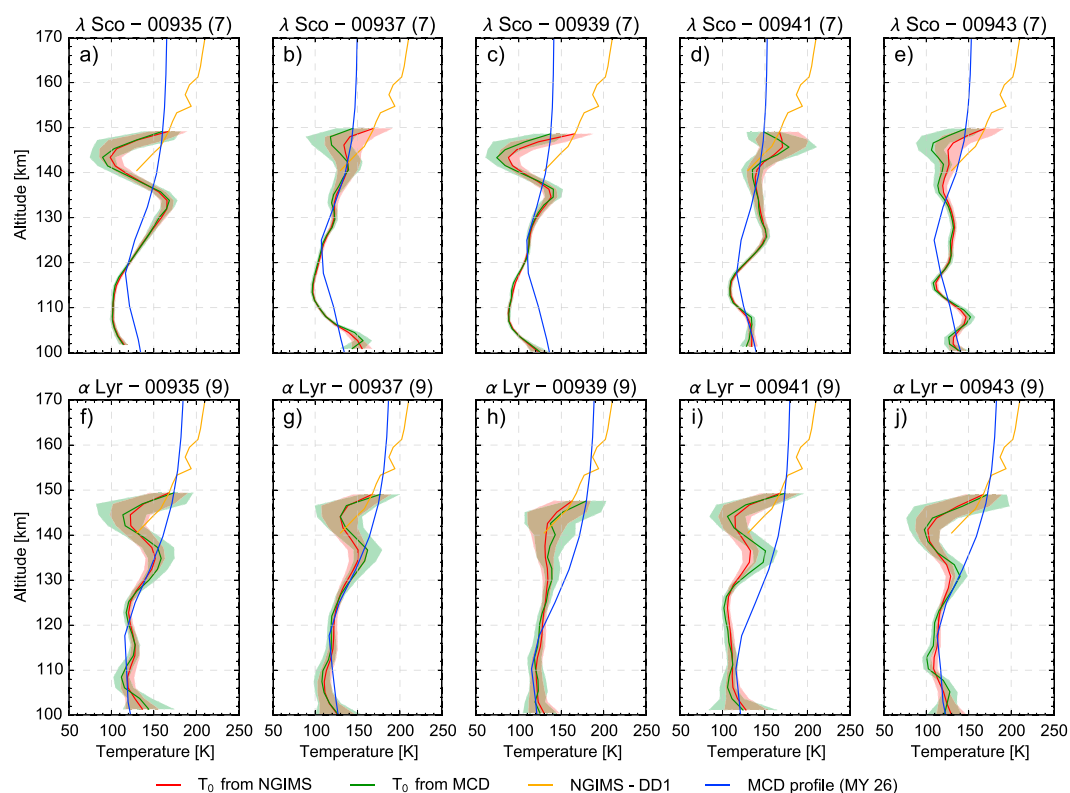
Figure 3. Temperature profiles inferred from the CO_2 densities. (a–j) Results from a single occultation. The red curves show temperature profiles calculated using the NGIMS profile [*Mahaffy et al.*, 2015] (yellow line) as upper boundary conditions. The green curves show temperature profiles calculated using the MCD profile [*Millour et al.*, 2014] (blue line) for the latitude, longitude, and local time of the occultation as upper boundary conditions. The shaded areas illustrate the uncertainties, calculated from the propagation of the errors from the density measurements.

altitudes. Better results are obtained by utilizing temperatures determined from NGIMS measurements during the first deep dip campaign to define the upper boundary [*Mahaffy et al.*, 2015]. During a deep dip, the lowest altitude of MAVEN periapse is roughly 125 km; ∼25 km lower than during normal science mapping. The solar zenith angle during this deep dip was close to 110°, roughly consistent with that for the occultations listed in Table 1. The NGIMS and IUVS occultation measurements are complimentary in the sense that NGIMS measures the atmosphere at lower pressures and IUVS occultations at higher pressures and, for the best occultations, the measurement regions nearly overlap. Using the NGIMS temperature as the upper boundary temperature produces the red curves in Figure 3. With either boundary conditions, most profiles exhibit significant departures from the MCD models.

To investigate this problem further, we show in Figure 4 the average temperature profiles for the λ Sco and α Lyr occultations and their uncertainties calculated as the standard deviation of the mean along with comparable averages from the MCD database. Repeated observations of a star sample different longitudes but similar latitudes and local times. We can therefore calculate a rough longitude coverage by taking the mean of all occultations of a star. We calculate the means on a pressure grid rather than an altitude grid to account for possible variations in the lower atmosphere. The average IUVS profiles are calculated using the NGIMS upper boundary condition. The averaging procedure removes longitude variations and much of the small-scale, wave-like structure in the profiles. The mean profiles obtained using the MCD upper boundary are quite similar (differences smaller than measurement uncertainty) and so are not shown in Figure 4.

The temperature profiles exhibit several interesting features. There is a temperature minimum at around 110 km, equivalent to ∼10^{-3} Pa, which is at a slightly higher pressure than the mesopause predicted by the MCD models. Throughout this region, from 100–125 km (from 10^{-2} to 10^{-4} Pa in pressure space), the measured and predicted temperatures are in fairly good agreement, with the measurements slightly colder, by less than 10–20 K, than the models. This difference is comparable with or even smaller than the variability in the
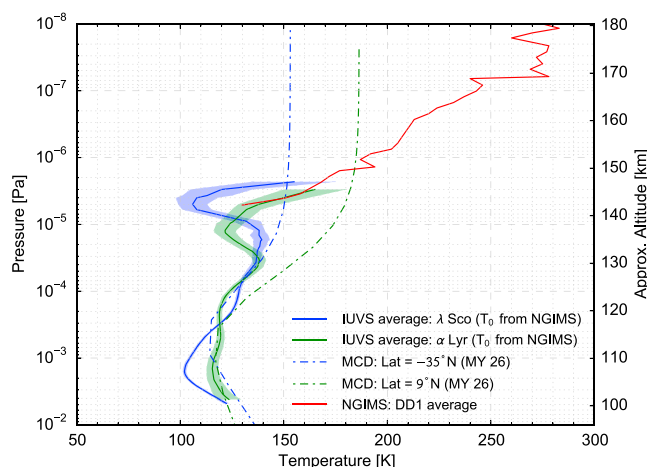
Figure 4. The average temperature profile for the λ Sco (blue) and α Lyr (green) occultations calculated using NGIMS (solid) to define the upper boundary temperature along with the average of the MCD (version 5.2) profiles [*Millour et al.*, 2014] (dashed) for this set of occultations. The blue and green shaded areas represent the uncertainties calculated as the standard deviation of the mean. NGIMS results [*Mahaffy et al.*, 2015] are shown as the red curve.

measured profiles. The standard deviation in this altitude range is between 10 and 25 K for the λ Sco occultations (latitude of −35°N) and around 10 K for α Lyr occultations (latitude of 9°N). Larger differences develop at higher altitudes. The model temperatures increase steadily from the mesopause, eventually reaching an exospheric temperature of 150 K and 190 K for mean latitudes of around −35°N and 9°N, respectively, while the measured temperatures decrease at pressures less than 3.5×10^{-5} Pa (around 135 km) reaching another minimum near 7×10^{-6} Pa (around 145 km). The difference between the average of the data and the average of the model at this level reaches 50 K, which corresponds to a difference up to 50% of the measured temperature.

A similar temperature difference was noted by *McDunn et al.* [2010], Figure 8, in their comparison of MEX/SPICAM occultation results to MGCM-MTGCM model [*Bougher et al.*, 2004, 2006, 2008]; however, the *McDunn et al.* [2010] analysis was limited to pressures greater than 10^{-4} Pa. Our results show that the difference continues to increase with decreasing pressure to the large values mentioned above. Eventually, as shown in the NGIMS profile, the atmospheric temperature increases to values of ~275 K, which is significantly higher than the exospheric temperature in the model, while the temperature rise occurs at significantly lower pressures than predicted by the MCD models. The differences shown here are similar in shape but much larger in magnitude than that between GCM predictions and temperatures derived from accelerometer measurements on the Mars Reconnaissance Orbiter [*Keating et al.*, 2008].

4. Summary and Discussion

The results reported here suggest that there is considerable variability in the temperature gradient in the lower thermosphere and that we do not yet adequately understand this region of the Mars atmosphere. The failure of the models to predict the structure of the thermosphere indicates that the energy balance in the models does not represent that of the Martian thermosphere. With the limited observations to date it is difficult to pinpoint the reason for the disagreement. This first campaign probed only the nightside. The temperatures in this region are maintained by the transport of heat from the dayside to nightside. The fact that the observed temperatures are cooler than predicted may indicate that the day-night flow is overestimated in the models. Alternatively, the radiative cooling rates in the atmosphere may be larger than that contained in the models causing the lower thermosphere to cool faster than predicted [*McDunn et al.*, 2010]. A more recent study by *Medvedev et al.* [2015] showed that enhanced CO_2 15 μm cooling due to elevated O densities together with gravity wave-induced cooling leads to temperature decreases of ~20 K at high latitudes and ~5 K at equatorial latitudes. Although significantly smaller than the discrepancies found here our results suggest that these mechanisms deserve further investigation. An important question is whether these cool nightside temperatures imply large day/night temperature differences at these levels or whether the lower thermosphere on the dayside is likewise surprisingly cool at these levels. If large day/night temperature differences do exist, they imply strong pressure forces that should alter the circulation of the upper atmosphere.

Finally, there is the question of whether the temperatures derived here are stable long-term features of the Martian atmosphere. Fortunately, future occultation campaigns will both probe the dayside atmosphere and further investigate the nightside, and we can look forward to observations shedding new light on this interesting discovery.

References

Bougher, S. W., S. Engel, D. P. Hinson, and J. R. Murphy (2004), MGS Radio Science electron density profiles: Interannual variability and implications for the Martian neutral atmosphere, *J. Geophys. Res.*, *109*, E03010, doi:10.1029/2003JE002154.

Bougher, S. W., J. M. Bell, J. R. Murphy, M. A. López Valverde, and P. G. Withers (2006), Polar warming in the Mars thermosphere: Seasonal variations owing to changing insolation and dust distributions, *Geophys. Res. Lett.*, *33*, L02203, doi:10.1029/2005GL024059.

Bougher, S. W., P.-L. Blelly, M. Combi, J. L. Fox, I. Mueller-Wodarg, A. Ridley, and R. G. Roble (2008), Neutral upper atmosphere and ionosphere modeling, *Space Sci. Rev.*, *139*(1), 107–141.

Capalbo, F. J., Y. Bénilan, R. V. Yelle, T. T. Koskinen, B. R. Sandel, G. M. Holsclaw, and W. E. McClintock (2013), Solar occultation by Titan measured by Cassini/UVIS, *Astrophys. J. Lett.*, *766*(2), L16, doi:10.1088/2041-8205/766/2/L16.

Forget, F., F. Montmessin, J.-L. Bertaux, F. González-Galindo, S. Lebonnois, A. Reberac, E. Dimarellis, and M. A. López-Valverde (2009), Density and temperatures of the upper Martian atmosphere measured by stellar occultations with Mars Express SPICAM, *J. Geophys. Res.*, *114*, E01004, doi:10.1029/2008JE003086.

González-Galindo, F., F. Forget, M. A. López-Valverde, M. Angelats i Coll, and E. Millour (2009), A ground-to-exosphere Martian general circulation model: 1. Seasonal, diurnal, and solar cycle variation of thermospheric temperatures, *J. Geophys. Res.*, *114*, E04001, doi:10.1029/2008JE003246.

Jakosky, B. M., et al. (2015), The Mars Atmosphere and Volatile Evolution (MAVEN) mission, *Space Sci. Rev.*, doi:10.1007/s11214-015-0139-x.

Keating, G., S. Bougher, R. A. M. Theriot, and R. Tolson (2008), Properties of the Mars upper atmosphere derived from accelerometer measurements, paper presented at 37th COSPAR Scientific Assembly, 1478 pp., Montréal, Canada, 13–20 Jul. [Available at http://adsabs.harvard.edu/abs/2008cosp...37.1478K.]

Koskinen, T. T., R. V. Yelle, D. S. Snowden, P. Lavvas, B. R. Sandel, F. J. Capalbo, Y. Benilan, and R. A. West (2011), The mesosphere and lower thermosphere of Titan revealed by Cassini/UVIS stellar occultations, *Icarus*, *216*(2), 507–534.

Lebonnois, S., E. Quémerais, F. Montmessin, F. Lefèvre, S. Perrier, J.-L. Bertaux, and F. Forget (2006), Vertical distribution of ozone on Mars as measured by SPICAM/Mars Express using stellar occultations, *J. Geophys. Res.*, *111*, E09S05, doi:10.1029/2005JE002643.

Lu, H. C., H. K. Chen, H. F. Chen, B. M. Cheng, and J. F. Ogilvie (2010), Absorption cross section of molecular oxygen in the transition $E^3\Sigma_u^- v = 0 - X^3\Sigma_g^- v = 0$ at 38 K, *Astron. Astrophys.*, *520*, A19, doi:10.1051/0004-6361/201013998.

Mahaffy, P. R., M. Benna, M. Elrod, R. V. Yelle, S. W. Bougher, S. W. Stone, and B. M. Jakosky (2015), Structure and composition of the neutral upper atmosphere of Mars from the MAVEN NGIMS investigation, *Geophys. Res. Lett.*, *42*, doi:10.1002/2015GL065329.

McClintock, W. E., N. M. Schneider, G. M. Holsclaw, J. T. Clarke, A. C. Hoskins, I. Stewart, F. Montmessin, R. V. Yelle, and J. Deighan (2014), The Imaging Ultraviolet Spectrograph (IUVS) for the MAVEN Mission, *Space Sci. Rev.*, doi:10.1007/s11214-014-0098-7.

McDunn, T. L., S. W. Bougher, J. Murphy, M. D. Smith, F. Forget, J.-L. Bertaux, and F. Montmessin (2010), Simulating the density and thermal structure of the middle atmosphere (~80–130 km) of Mars using the MGCM-MTGCM: A comparison with MEX/SPICAM observations, *Icarus*, *206*(1), 5–17.

Medvedev, A. S., F. González-Galindo, E. Yiğit, A. G. Feofilov, F. Forget, and P. Hartogh (2015), Cooling of the Martian thermosphere by CO_2 radiation and gravity waves: An intercomparison study with two general circulation models, *J. Geophys. Res. Planets*, *120*, 913–927, doi:10.1002/2015JE004802.

Millour, E., et al. (2014), A new Mars Climate Database v5.1, in *The Fifth International Workshop on the Mars Atmosphere: Modelling and Observation, held in Oxford, 13–16 January*, edited by F. Forget and E. Millour, 1301 pp.

Montmessin, F. (2013), Transport-driven formation of a polar ozone layer on Mars, *Nat. Geosci.*, *6*(11), 1–4.

Montmessin, F., F. Forget, J.-L. Bertaux, E. Quémerais, O. I. Korablev, S. Perrier, D. Fussen, S. Lebonnois, A. Reberac, and E. Dimarellis (2006a), Subvisible CO_2 ice clouds detected in the mesosphere of Mars, *Icarus*, *183*(2), 403–410.

Montmessin, F., E. Quémerais, J.-L. Bertaux, O. Korablev, P. Rannou, and S. Lebonnois (2006b), Stellar occultations at UV wavelengths by the SPICAM instrument: Retrieval and analysis of Martian haze profiles, *J. Geophys. Res.*, *111*, E09S09, doi:10.1029/2005JE002662.

Minschwaner, K., G. P. Anderson, L. A. Hall, and K. Yoshino (1992), Polynomial coefficients for calculating O_2 Schumann-Runge cross sections at 0.5 cm^{-1} resolution, *J. Geophys. Res.*, *97*(D9), 10,103–10,108.

Nier, A. O., and M. B. McElroy (1977), Composition and structure of Mars' upper atmosphere—Results from the neutral mass spectrometers on Viking 1 and 2, *J. Geophys. Res.*, *82*(28), 4341–4349.

Ogawa, S., and M. Ogawa (1975), Absorption cross sections of $O_2(a^1\Delta_g)$ and $O_2(X^3\Sigma_g^-)$ in the region from 1087 to 1700 Å, *Can. J. Phys.*, *53*(19), 1845–1852.

Parkinson, W. H., J. Rufus, and K. Yoshino (2003), Absolute absorption cross section measurements of in the wavelength region 163–200 nm and the temperature dependence, *Chem. Phys.*, *290*(2–3), 251–256.

Quémerais, E., J.-L. Bertaux, O. Korablev, E. Dimarellis, C. Cot, B. R. Sandel, and D. Fussen (2006), Stellar occultations observed by SPICAM on Mars Express, *J. Geophys. Res.*, *111*, E09S04, doi:10.1029/2005JE002604.

Sandel, B. R., H. Gröller, R. V. Yelle, T. Koskinen, N. K. Lewis, J.-L. Bertaux, F. Montmessin, and E. Quémerais (2015), Altitude profiles of O2 on Mars from SPICAM stellar occultations, *Icarus*, *252*, 154–160.

Snowden, D., R. V. Yelle, J. Cui, J. E. Wahlund, N. J. T. Edberg, and K. Ågren (2013), The thermal structure of Titan's upper atmosphere. I: Temperature profiles from Cassini INMS observations, *Icarus*, *226*(1), 552–582.

Stark, G., K. Yoshino, P. L. Smith, and K. Ito (2007), Photoabsorption cross section measurements of CO_2 between 106.1 and 118.7 nm at 295 and 195 K, *J. Quant. Spectros. Radiat. Transfer*, *103*(1), 67–73.

Yoshino, K., Y. Sun, J. R. Esmond, W. H. Parkinson, K. Ito, and T. Matsui (1996), Absorption cross section measurements of carbon dioxide in the wavelength region 118.7–175.5 nm and the temperature dependence, *J. Quant. Spectros. Radiat. Transfer*, *55*(1), 53–60.

Yoshino, K., W. H. Parkinson, K. Ito, and T. Matsui (2005), Absolute absorption cross-section measurements of Schumann-Runge continuum of O_2 at 90 and 295 K, *J. Mol. Spectrosc.*, *229*(2), 238–243.